Lawrence Berkeley National Laboratory
Recent Work

Title
Solution-Synthesized High-Mobility Tellurium Nanoflakes for Short-Wave Infrared Photodetectors.

Permalink
https://escholarship.org/uc/item/37d2q8jk

Journal
ACS nano, 12(7)

ISSN
1936-0851

Authors
Amani, Matin
Tan, Chaoliang
Zhang, George
et al.

Publication Date
2018-07-01

DOI
10.1021/acsnano.8b03424

Peer reviewed

Solution-Synthesized High-Mobility Tellurium Nanoflakes for Short-Wave Infrared Photodetectors

Matin Amani, [#,1,2], Chaoliang Tan [#,1,2], George Zhang[1,2], Chunsong Zhao[1,2,3], James Bullock[1,2], Xiaohui Song[3,4], Hyungjin Kim[1,2], Vivek Raj Shrestha[5], Yang Gao[6], Kenneth B. Crozier[5,6], Mary Scott[3,4], and Ali Javey[1,2,*]

[1]Electrical Engineering and Computer Sciences, University of California at Berkeley, Berkeley, CA 94720, United States
[2]Materials Sciences Division, Lawrence Berkeley National Laboratory, Berkeley, CA 94720, United States
[3]Department of Materials Science and Engineering, University of California at Berkeley, Berkeley, CA 94720, United States
[4]The Molecular Foundry, Lawrence Berkeley National Laboratory, Berkeley, CA, 94720
[5]School of Physics, University of Melbourne, VIC 3010, Australia
[6]Department of Electrical and Electronic Engineering, University of Melbourne, Victoria 3010, Australia

*Address correspondence to ajavey@eecs.berkeley.edu
[#]These authors contribute equally to this work.

Keywords: tellurium, 2D materials, solution-synthesized, high-mobility, short-wave infrared, photodetectors

Abstract

Two-dimensional (2D) materials, particularly black phosphorous (bP), have demonstrated themselves to be excellent candidates for high-performance infrared photodetectors and transistors. However, high-quality bP can be only obtained *via* mechanical exfoliation from high temperature- and high-pressure-grown bulk crystals and degrades rapidly when exposed to ambient conditions. Here, we report solution-synthesized and air-stable quasi-2D tellurium (Te) nanoflakes for short-wave infrared (SWIR) photodetectors. We

34 perform comprehensive optical characterization *via* polarization-resolved

35 transmission and reflection measurements, and report the absorbance and

36 complex refractive index of Te crystals. It is found that this material is an

37 indirect semiconductor with a bandgap of 0.31 eV. From temperature-

38 dependent electrical measurements, we confirm this bandgap value and find

39 that 12 nm thick Te nanoflake show high hole mobilities of 450 and 1430 cm^2

40 V^{-1} s^{-1} at 300K and 77K, respectively. Finally, we demonstrate that despite its

41 indirect bandgap, Te can be utilized for high-performance SWIR

42 photodetectors by employing optical cavity substrates consisting of Au/Al_2O_3

43 to dramatically increase the absorption in the semiconductor. By changing

44 the thickness of the Al_2O_3 cavity, the peak responsivity of Te

45 photoconductors can be tuned from 1.4 μm (13 A/W) to 2.4 μm (8 A/W) with

46 a cut-off wavelength of 3.4 μm, fully capturing the SWIR band. An optimized

47 room temperature specific detectivity (D*) of 2×10^9 cm $Hz^{1/2}$ W^{-1} is obtained

48 at a wavelength of 1.7 μm.

49

50   Narrow bandgap semiconductors, with bandgaps in the range of 0.7 to

51 0.3 eV, have been heavily investigated for numerous applications. These

52 include high-speed and high-performance transistors, which typically require

53 materials with high mobility and low effective mass.[1,2] Additionally,

54 photodetectors and light sources which can operate in the short-wave

55 infrared (SWIR, 1.4 μm – 3 μm) band are heavily utilized for imaging and

56 optical communication.[3-5] This area has typically been dominated by III-V

57 semiconductors such as indium gallium arsenide (InGaAs) and indium

2

58 gallium arsenide phosphide (InGaAsP), which have excellent performance but

59 require complex growth and fabrication procedures.[6,7] Numerous research

60 groups have investigated techniques to achieve III-V semiconductors through

61 non-epitaxial growth on silicon or by layer transfer.[8-11] However, these

62 techniques still introduce significant complexity and may require high growth

63 temperature. Moreover, key limitations still exist in InGaAs-based devices; an

64 example being edge-recombination in scaled InGaAs photodiodes which

65 limits pixel sizes in focal plane arrays to dimensions of 5-6 μm, well above

66 the diffraction limit.[12] As such, there is a pressing need to find suitable

67 materials that can either improve the performance and/or reduce the costs

68 of these devices.

69   One such potential material system is two-dimensional (2D) materials,

70 which have been heavily studied over the past decade. One of the key

71 advantages of 2D materials, which enables their high performance, is their

72 naturally terminated surfaces; *i.e.* since the out-of-plane bonds in these

73 materials are van der Waals rather than covalent.[13,14] As such, they do not

74 suffer from the surface-induced performance degradation commonly

75 observed in three-dimensional (3D) semiconductors, which require surface

76 passivation (typically in the form of cladding layers). This has enabled

77 extraordinary electronic and optical properties of these materials such as

78 photoluminescence quantum yields approaching unity and their exceptional

79 thickness scalability down to the monolayer limit.[15,16] Devices which have

80 exploited the advantages and physics of 2D systems have demonstrated

81 dramatic scaling as well as new devices paradigms.[17-19] However, edges in 2D

82   layers still act as recombination centers and are analogous to a surface in a

83   3D crystal structure.[20] A recent work by Wang *et al.* demonstrated the

84   solution synthesis of air-stable quasi-2D Te nanosheets and its high-

85   performance for field-effect transistors.[21] Note that Te is a true one-

86   dimensional (1D) system, which can potentially overcome some of these

87   limitations since it consists of van der Waals bonded molecular chains.[22] As

88   such these material systems naturally possess no dangling bonds when

89   scaled, with the exception of the ends of the molecular chains.[22] Importantly,

90   this material also possesses a small, thickness tunable bandgap enabling its

91   potential use in SWIR photodetectors. Recent theoretical works have

92   predicated an indirect gap of 0.35 eV in bulk and a direct gap of 1.04 eV in

93   the monolayer case.[23,24]

94   Here, we systematically study the optical and electrical properties of

95   solution-synthesized quasi-2D Te nanoflakes. From polarization-resolved IR

96   transmission and reflection measurements, we experimentally extract the

97   bandgap, absorbance, and complex refractive index of this material.

98   Temperature-dependent electrical measurements were performed to verify

99   the optically measured bandgap values as well as determine the carrier

100 transport properties as a function of temperature in quasi-2D Te nanoflakes.

101 Finally, we demonstrate SWIR photoconductive detectors based on thin (16-

102 20 nm) quasi-2D Te nanoflakes. Although this material has low absorbance in

103 the SWIR (6×10^5 cm^{-1} for wavelengths in the range of 2 to 3.5 μm) induced

104 by the indirect bandgap, the Te nanoflake-based photodetectors exhibit high

105 photoresponsivity and specific detectivity by leveraging optical cavities

4

106 engineered to maximize absorption at various technologically important

107 wavelengths in the SWIR range.

108 **RESULTS and DISCUSSION**

109 **Material Synthesis and Characterization.**

110   Quasi-2D Te nanoflakes with varying thickness in the range of 10-200

111 nm were synthesized by a hydrothermal method *via* reduction of sodium

112 tellurite with hydrazine hydrate in the presence of poly(-vinyl pyrrolidone) in

113 an aqueous alkaline solution at 180℃ for certain varying times (details are

114 provided in methods).[21,25] The crystal structure of Te is shown in Figure 1a-c.

115 The Te crystallizes in a structure composed of Te atomic chains in a

116 triangular helix that are stacked together *via* van der Waals forces in a

117 hexagonal array (Figure 1a). In this structure, Te atoms only form covalent

118 bonds to the two nearest neighbor Te atoms in the helical chain (Figure 1b).

119 Therefore, Te is a true 1D system rather than a 2D van der Waals crystal.

120 When it is viewed from x-axis, the zig-zag layers are seen to be stacked

121 together *via* van der Waals forces to form a 3D structure (Figure 1c). Figure

122 1d shows the transmission electron microscope (TEM) image of a typical Te

123 nanoflake with a length of 15 µm and width of 4 µm. The corresponding high-

124 resolution TEM (HR-TEM) image shows the continuous crystal lattice of the Te

125 nanoflake and the measured the lattice constant is ~2 Å (Figure 1e), which is

126 assignable to the (003) planes of the Te crystal. The corresponding selected

127 area electron diffraction (SAED) pattern of the Te nanoflake shows bright

128 diffraction spots with a rectangular shape, in which the nearest two spots to

129   the diffraction center correspond to the (110) and (001) planes of the Te

130   crystal (Figure 1f). Both the HR-TEM and SAED pattern results indicate that

131   the solution-synthesized Te nanoflake is single-crystalline. The optical image

132   shows that Te nanoflakes have an irregular shape with length of tens of

133   micrometers, width of few micrometers and thickness of 10-30 nm (Figure

134   2a). Note that there are always some Te nanowires along Te nanoflakes in

135   the growth solution, but Te nanowires can be partially removed from the

136   solution by proper centrifugation (see the details in Methods). An atomic

137   force microscope (AFM) image of a Te nanoflake with a thickness of 16.1 nm

138   is shown in Figure 2b. Raman spectrum of tellurium nanoflakes gives three

139   vibrational modes at 92, 121, 141 cm^{-1} (Figure 2c) corresponding to the E_1-

140   TO, A_1, and E_2 peaks, which are consistent with previous literature

141   reports.[21,26] The X-ray diffraction (XRD) peaks of Te nanoflakes match well

142   with the simulated reference (Figure 2d). Both Raman and XRD analysis

143   further confirm the successful preparation of Te nanoflakes.[21,25]

144   **Electrical Properties.**

145   We now turn our attention to the electrical properties and performance

146   of the quasi-2D Te nanoflakes. To this end, back-gated field-effect transistors

147   were fabricated on Si/50 nm SiO_2 by patterning Pd (40 nm thick) electrodes

148   on Te nanoflakes with thickness ranging from 10-20 nm using electron-beam

149   lithography.[21] The I_d-V_d characteristics of a 12.3 nm thick quasi-2D Te field-

150   effect transistor, as well as an optical image of the measured device (L = 6.8

151   μm, W = 1.5 μm, where L and W are length and width respectively) are

152   shown in Figure 3a. The device shows dominantly p-type transport

153 characteristics and a peak current density of 116 µA/µm at a V_d = -1 V and V_g

154 = -20 V. It should be noted that in some devices (Figure S1) ambipolar

155 transport characteristics are observed, indicating that *via* proper contact

156 engineering n-type transport could be obtained. Additionally, this device

157 shows a current on/off ratio of ~3×10³, which is expected for a material with

158 a small bulk bandgap of ~0.31 eV. The output characteristics of this device

159 are shown in Figure 3b, and show current saturation at high drain bias, as

160 well as linear behavior at low drain biases, indicating low contact resistance.

161 We then utilize the square law model to calculate the effective mobility (μ_{Eff})

162 in this device as a function of gate field (Figure 3c) using $\mu_{Eff}=(dI_d/dV_d)/¿¿$,

163 where C_{ox} is the gate capacitance (69.1 nF cm^{-2} in the case of 50 nm SiO$_2$)

164 and V_t is the threshold voltage. We extract a high peak μ_{Eff} of 619 cm^{2}V^{-1}s^{-1}

165 for holes, which is very competitive with high-performance p-type

166 semiconductors with similar bandgaps such as InGaSb and bP, especially

167 considering that the material is prepared by a solution-based method.[27-29]

168 The thickness-dependent transport properties of quasi-2D Te nanoflakes

169 were also investigated over a range of 11 to 36 nm as shown in Figure 3d

170 and 3e. As the overall thickness of the Te nanoflakes is reduced a dramatic

171 improvement in the ratio of the on/off currents from ~30× to ~4000× can be

172 observed, which can be attributed to reduced gating efficiency in the device.

173 Furthermore, over this measured thickness range, we find that there is

174 negligible variation in the peak effective mobility which has an average value

175 of 424±74 cm^{2}V^{-1}s^{-1} over thirty-nine measured samples.

176   To better understand the transport in this material, we performed

177   temperature-dependent electrical characterization of the devices. I_d-V_g

178   characteristics of quasi-2D Te nanoflakes with different thicknesses

179   measured over a temperature range of 77K to 350K are shown in Figure 4a

180   and Figure S1. A clear increase in the current on/off ratio can be observed

181   when the device is cooled, which is consistent with small bandgap materials,

182   where thermal generation dramatically increases the carrier densities at

183   elevated temperatures. From the temperature-dependent measurements, we

184   extract the μ_Eff at a gate overdrive of -10 V as a function of temperature for

185   different layer thicknesses as shown in Figure 4b. For all thicknesses, the

186   mobility increases as the temperature is reduced, with the 12 nm thick

187   device showing a μ_Eff of 1430 and 450 cm^{2}V^{-1}s^{-1} at 77K and 300K respectively.

188   For all three thicknesses, we observe the temperature dependence of

189   mobility can be fitted with a power law, $\mu_\text{Eff} \propto T^{-\gamma}$, where γ = -1.03 in our case.

190   This indicates that the mobility in this material is limited by phonon

191   scattering and not ionized impurities.[30] Additionally, we estimate the

192   bandgap using temperature-dependent measurements on a device prepared

193   on a 260 nm gate oxide. In this case, the minimum drain currents, $I_\text{d,min}$, is

194   determined by thermal activation of carriers over the contact Schottky

195   barrier height.[31] The resulting data, shown in Figure 4c, can be fit using:

196    $I_{d,min} \propto \exp\left(-E_g/kT\right)$

197   where T is the temperature, E_g is the transport bandgap, and k is the

198   Boltzmann constant. We extract an E_g of 280 meV for a 11.8 nm thick

199 sample, and it is important to note that this method is expected to

200 underestimate the bandgap due to contributions from trap states.

201 **Optical Properties.**

202 To identify the optical bandgap of the quasi-2D Te nanoflakes, we

203 performed polarization-resolved transmission and reflection measurements

204 on Te nanoflakes which were transferred onto KBr. Polarization-resolved

205 transmission and reflection spectra measured on a 111 nm thick sample are

206 shown in Figure 5a. In order to accurately extract the absorption in the

207 sample, the optical path was kept constant for both the transmission and

208 reflection measurements, as annotated in the Figure 5a. Transmission and

209 reflection spectra were taken in reference to the blank KBr substrate and an

210 Au mirror, respectively. The total absorption and the corresponding

211 absorption coefficient in the material can then be calculated as 100%-

212 Reflection-Transmission as shown in Figure 5b and 5c. For light polarized

213 along the direction of the Te molecular wires (defined as 90°), we measure a

214 strong absorption that can be fitted to a direct bandgap (Figure 5c and

215 Figure S2) at 0.71 eV. However, when the light is polarized perpendicular to

216 the axis of the Te molecular wires (defined as 0°) a significantly weaker

217 absorption edge is observed at lower wavelengths. From similar analysis, the

218 transition can be fitted to an indirect bandgap at 0.31 eV. Importantly, while

219 the absorption coefficient for wavelengths below 1.6 μm is high (4.5×10^6 cm$^-$

220 ^{1}), the absorption for longer wavelengths (1.6 μm < λ < 3.4 μm) is an order

221 of magnitude lower (6×10^5 cm^{-1}). As such, in order to effectively utilize this

222 material in the full SWIR band, it is necessary to increase the absorption *via*

223 proper optical engineering.[32]

224   To this end, we extracted the complex refractive index (n, k) which can

225 be used to estimate the total absorption in the quasi-2D Te layers in

226 combination with optical cavities, back-reflectors, or anti-reflection coatings.

227 The refractive index was extracted using a previously established technique

228 for nanoscale materials for unpolarized light, where reflection is measured as

229 a function of oxide or sample thickness.[33] In our case, quasi-2D Te nanoflakes

230 of thicknesses varying from 16 nm to 180 nm were drop-casted on Au

231 substrates, and the reflection spectra were measured using an Fourier

232 transform infrared spectrometer (FTIR). The resulting reflection data are

233 plotted as a function of thickness and wavelength. (Figure 6a and Figure S3).

234 To extract the complex refractive index from the reflection measurements,

235 we utilize the transfer matrix method to fit a refractive index to the

236 measured reflection *versus* thickness at each wavelength.[34] The extracted n

237 and k values are plotted in Figure 6b; the extracted extinction coefficient

238 clearly shows absorption resulting from both the indirect and direct

239 transitions at the expected wavelengths and corroborates the results from

240 absorption measurements shown in Figure 5c.

241 **Optical Cavity Enhanced Gated-Photoconductors.**

242   Based on the optical properties and electrical properties of quasi-2D

243 Te, the device structure shown in Figure 7a was chosen to optimize

244 photoconductive detectors targeting the SWIR spectrum. Here, we selected

245 thicknesses in the range of 16-20 nm for the quasi-2D Te layers, which

246 provides desired   electrical characteristics, the most important of which

247 being a low dark current.[35] To increase the absorption, an optical cavity

248 consisting of an optically thick Au film (100 nm) and an Al_2O_3 dielectric

249 spacer layer was utilized. The predicted absorption for an 18 nm thick Te

250 layer as a function of wavelength and Al_2O_3 thickness was calculated using

251 the transfer matrix method and is shown in Figure 7b. From these

252 simulations, it can be clearly seen that by adjusting the thickness of the Al_2O_3

253 layer, the peak absorption wavelength can be tuned over a large range and

254 the total absorption in the material can be increased by over two orders of

255 magnitude relative to a sample on Si/SiO_2 (Figure S4). Additionally, the

256 optical cavity simultaneously acts as the gate stack in this structure.

257   Figure 7c shows optical images of devices fabricated on three different

258 Al_2O_3 spacer thickness (550 nm (i), 150 nm (ii), and 350 nm (iii)), which are

259 selected to provide optimized absorption at 1.4 μm, 1.8 μm, and 2.2 μm,

260 respectively (reflection spectra of devices on these substrates are shown in

261 Figure S5). The spectral responsivity of these devices to SWIR illumination

262 was characterized using an FTIR, by placing the devices in place of the

263 internal detector and focusing the light source of the FTIR on the device with

264 a CaF_2 lens. To calibrate the measurements, the internal Deuterated

265 Triglycine Sulfate (DTGS) in the FTIR, which has a wavelength independent

266 responsivity, was used to determine the relative intensity of the light source

267 while a NIST traceable Ge photodiode was used to determine the absolute

268 intensity of the illumination (further measurement details are provided in the

269 methods and ref. 35). The final responsivity (R) is then calculated as $R(\lambda) =$

270    $I_{ph}(\lambda)/P_{in}(\lambda)$, where I_{ph} is the photocurrent and P_{in} is the incident optical power

271   on the device. The spectral responsivity for representative devices fabricated

272   on the three different optical cavity substrates are shown in Figure 7d.

273   Devices fabricated on these three substrates were measured at a drain bias

274   of V_d = 5 V, and the gate voltage was adjusted to maximize the responsivity.

275   The measured responsivity curves closely match the calculated absorption

276   curves which further confirms the estimated refractive index values.

277   **Gate-dependent Photoresponse, Detectivity, and Frequency**

278   **Response.**

279   To further characterize the performance of these photodetectors,

280   additional measurements were performed on an 18.8 nm thick device

281   fabricated on a Au/150 nm Al_2O_3 substrate. The I_d-V_g characteristics of a

282   device measured at 78K and 297K without the presence of a cold shield is

283   shown in Figure 8a. The gate and drain bias dependence of the device at an

284   incident wavelength of 1.7 μm are shown in Figure 8b and 8c, respectively.

285   We can see that the photoresponse can be strongly modulated by the gate

286   bias and is maximized when the device is biased such that drain current is

287   minimized, similar to what has previously been observed in bP

288   photoconductors[35,36]. This can be seen in the clear peak responsivity of 27 A/

289   W at 78K, while the responsivity at 297K saturates with increasing gate

290   biases to a peak measured value of 16 A/W. Additionally, the device shows

291   an approximately linearly increasing responsivity at low V_d, and begins to

292   show saturation at high V_d. The full spectral responsivity of the device is

293 shown in Figure 8d. For V_d = 5 V, this detector shows a peak responsivity at λ

294 = 1.7 μm of 27 A/W and 16 A/W at 78K and 297K, respectively.

295   To calculate the specific detectivity of this device, the noise current

296 density is measured under bias conditions which give maximum responsivity

297 at an integration time (Δf) of one second and is shown in Figure 8e. The

298 noise currents clearly show the expected 1/f (where f is frequency) flicker

299 noise which is typically attributed to charge trapping/de-trapping. Utilizing

300 the   noise   and   responsivity   measurements,   we   calculate   the   specific

301 detectivity (D^*) using:

302 $$D^{\mathbf{\iota}}=\frac{\sqrt{A\,\Delta f}}{NEP}=\frac{R\sqrt{A\,\Delta f}}{i_n}$$

303 where A is the detector area, NEP is noise equivalent power, and i_n is the

304 noise current. In the ideal case for photoconductors, the i_n is limited by shot

305 noise and can be calculated from dark current using: $\langle i_S^2 \rangle = 2\,q\,I_{G-R}\,\Delta f$.[37,38] This

306 typically   overestimates   noise   current;   thus,   we   utilized   the   experimental

307 noise currents taken at a modulation frequency of 1 kHz, which was selected

308 to   minimize   the   contribution   of   1/f noise.   The   specific   detectivity   as   a

309 function of wavelength is shown in Figure 8f for both 78K and 297K. At room

310 temperature these devices show a peak D^* of 2.9×10^9 cmHz$^{1/2}$W^{-1}. This value

311 dramatically increases at low temperatures due to the large decrease in the

312 noise   current   as   well   as   the   improved   responsivity   to   a   peak   value   of

313 2.6×10^{11} cmHz$^{1/2}$W^{-1}.

314   To characterize the speed of this device, a directly modulated laser

315 diode (λ = 1.55 μm) was utilized to excite the photoconductor. The response

316 of the device to a low-frequency and high-frequency square wave are shown

317 in Figure 9a and 9b, respectively. From both of the step responses shown in

318 Figure 9a and 9b, a slow and fast component of the rise/fall time can be

319 observed. To more clearly characterize this behavior, the photoresponse was

320 measured with a sinusoidally modulated incident light over a wide frequency

321 range (100 mHz to 100 kHz) as shown in Figure 9c. Over this measured

322 spectral range, a clear 3dB cutoff wavelength cannot be observed, indicating

323 that it is higher than the measured range. However, the device shows a

324 weak increase in response for light modulated at low frequencies; *i.e.* the

325 photoresponse at a 100 kHz shows only a ~5× drop relative to the low

326 frequency (~0.1 Hz) photoresponse. It is likely that this behavior is a result

327 of photoconductive gain present in the device which consistent with the high

328 responsivity and the short carrier transit time (τ_{tr}), which is calculated to be

329 0.4 ns according to $\tau_{tr} = L^2/(\mu V_d)$, where L is channel length (8.9 μm) and μ in

330 this case is 392 $cm^2V^{-1}s^{-1}$. The exact mechanisms of the gain likely is a result

331 of the population and depopulation of trap states, which show saturation at

332 high illumination powers.[39-41] This is particularly likely given the fact that the

333 Te nanoflakes in this work were prepared using solution-based synthesis.

334 **Polarization-Resolved Photoresponse.**

335   Finally, we investigated the polarization-dependent photoresponse of

336 Te nanoflake-based photodetectors. We chose a device fabricated on a 350

337 nm thick Al_2O_3 substrate as an example to measure the responsivity, which

338 provides strong absorption enhancement at wavelengths covering indirect

339 gap band edge. Figure 10a shows the responsivity of an 18.8 nm thick Te

340 photoconductor measured at various incident polarization angles, with 0°

341 and 90° corresponding to light polarized perpendicular and parallel to the

342 molecular wires, respectively. A clear drop in the responsivity for

343 wavelengths greater 1.5 µm can be observed when the incident light is

344 polarized at 90°, consistent with the indirect band edge. A polar plot showing

345 the responsivity as a function of polarization at wavelengths of 3 µm and 1.5

346 µm is shown in Figure 10b, and clearly shows the highly anisotropic

347 responsivity of the indirect gap, while the direct gap shows minimal

348 dependence on the polarization of the light.

349 **CONCLUSION**

350   In summary, we have performed a systematic study on the electrical

351 and optical properties of solution-synthesized quasi-2D Te, an indirect, small

352 bandgap (0.31 eV) semiconductor. The Te nanoflake-transistor shows high

353 effective hole mobilities of 450 and 1430 cm^2 V^{-1} s^{-1} at 300K and 77K

354 respectively. The absorbance and complex refractive index of Te were also

355 extracted based on the polarization-resolved transmission and reflection

356 measurements. Furthermore, the Te gated photodetectors exhibit high

357 responsivities over the entire SWIR range with a cut-off wavelength of 3.4

358 µm. Importantly, using the extracted optical parameters, we dramatically

359 enhanced the responsivity and specific detectivity of Te photodetectors

360 using optical cavity substrates. We show that the peak wavelength can be

361 tuned from 1.4 to 2.4 µm by changing the thickness of the Al_2O_3 cavity on

362 Au. This simple substrate engineering technique can be a general way to

363 significantly enhance the performance of other 2D material-based

364　photodetectors. In addition, due to the anisotropic crystal structure of the Te

365　nanoflakes, the devices possess a polarization-sensitive SWIR

366　photoresponse. Our electrical and optoelectronic study indicate that Te is a

367　promising material for high-performance and low-cost electronic and

368　optoelectronic devices. Finally, this material has a high potential for wafer-

369　scale production either through the assembly of solution-processed

370　nanoflakes to form semi-continuous thin films or through techniques such as

371　chemical vapor deposition or epitaxial growth.

372　**METHODS**

373　**Chemicals**

374　Sodium tellurite (Na_2TeO_3), hydrazine monohydrate ($N_2H_4 \cdot H_2O$) and

375　ammonium hydroxide solution ($NH_3 \cdot H_2O$, 28%) were purchased from Sigma-

376　Aldrich (USA). Poly(-vinyl pyrrolidone) (PVP, average M.W. 58,000) was

377　purchased from Alfa Aesar (USA). All the chemicals were used as received

378　without further purification. Milli-Q water (Milli-Q System, Millipore) was used

379　in all experiments.

380　**Synthesis of tellurium nanoflakes**

381　Tellurium nanoflakes were synthesized by a hydrothermal method according

382　to a previously reported procedure with slight modifications.[21,25] In a typical

383　procedure, 1.5 g of PVP was first dissolved in 16 mL DI water and 46 mg of

384　Na_2TeO_3 was then added and dissolved into the PVP solution to form a clear

385　solution. Then, 1.66 mL of ammonium hydroxide solution and 0.838 mL of

386　hydrazine monohydrate was added into the above solution in sequence. The

387　solution was then transferred into a 25 mL Teflon-lined stainless steel

388 autoclave. The autoclave was sealed well and then placed in an oven. The

389 autoclave was heated up to 180℃ from room temperature with ramp rate of

390 3 ℃/min and then maintained at 180℃ for 4 hours. After, the autoclave was

391 removed from the oven and cooled to room temperature by running water

392 immediately. The resulting product was purified and washed with DI water

393 three times by centrifugation at 3000 r.p.m for 2 min. After washing and

394 purification, the final tellurium solution is a silver-gray color. Note that there

395 are always some Te nanowires coexisting along with Te nanoflakes and it is

396 challenging to fully separate the nanowires from the nanoflakes. The final

397 product was redispersed in pure ethanol before being transferred to the

398 target substrate for characterization and device fabrication by drop-casting.

399 Maintaining the autoclave in oven at 180℃ for 4h will produce the tellurium

400 nanoflakes with a typical thickness in the range of 10-30 nm, with typical

401 lateral dimensions of 10-50 μm. It is important to point out that the thickness

402 of tellurium nanoflakes can be roughly controlled by controlling the reaction

403 time (4-30 hours) at 180℃. The thickness of tellurium nanoflakes can be

404 increased by prolonging the reaction.

405 **Device Fabrication**

406 Te nanoflakes were transferred onto p^{++} Si/SiO$_2$ chips with a 50 nm oxide or

407 back reflector Al$_2$O$_3$/Au chips with varying thicknesses of Al$_2$O$_3$ by drop-

408 casting the tellurium ethanol solution. Back reflector substrates were

409 prepared by evaporating Ti/Au/Ti (10 nm/200 nm/1 nm) on Si substrates,

410 followed by atomic layer deposition of Al$_2$O$_3$ (Cambridge Nanotech). The final

411 Al$_2$O$_3$ thickness was determined by ellipsometry. Suitable Te nanoflakes were

then located on an optical microscope and devices were fabricated using standard e-beam lithography techniques. After development, 40 nm thick Pd was evaporated as electrode contacts *via* e-beam evaporation and lift-off was performed using acetone.

Material Characterization

Transmission electron microscopy (TEM) images were performed at the National Center for Electron Microscopy at Laurence Berkeley National Laboratory using a FEI Titan 60–300 microscope operated at 200kV. Tapping mode atomic force microscope (AFM) measurements were conducted on a Dimension ICON AFM (Bruker, Germany) under ambient conditions. A AXS D8 Discover GADDS X-ray diffractometer (Bruker, Germany) equipped with a Vantec-500 area detector and a Co Kα (λ=1.7903 Å) X-ray source was used to measure the powder X-ray diffraction (XRD) pattern. The Raman spectrum was measured on Horiba Jobin Yvon LabRAM ARAMIS automated scanning confocal Raman microscope system with the excitation line of 532 nm (Horiba, Ltd. Japan). The Raman band of a silicon wafer at 520 cm^{-1} was used as the reference to calibrate the spectrometer.

Optical/Electrical Characterization

Samples for absorption/reflection measurements were transferred onto KBr substrates using a previously established dry transfer technique and were measured in an FTIR microscope (ThermoFisher).[35] Electrical measurements were performed in a cryogenic protestation (LakeShore) with a B1500a Semiconductor Parameter Analyzer (Agilent). Spectral photoresponse measurements were performed in a FTIR spectrometer (ThermoFisher) with a

436 customized Janis cryostat equipped with a CaF_2 window. Devices were wire

437 bonded in a 24 pin chip carrier and evacuated to a base pressure of $< 10^{-5}$

438 Torr. The cryostat was then placed at the auxiliary exit port of the FTIR, and

439 the exciting illumination from the tungsten lamp source was focused on the

440 sample using either a CaF_2 lens or a 15× Schwarzschild objective. The optical

441 velocity of the FITR was set to either 0.1515 or 0.4747 cm s^{-1}; the resulting

442 modulation frequency range (7.5 kHz to 300 Hz) is within the operating

443 regime of the frequency response. The photocurrent from the Te devices was

444 then sent to a current amplifier (Stanford Research Systems), which also

445 provided the bias voltage. The resulting signal was subsequently returned to

446 the external detector interface of the FTIR. The relative intensity of the

447 illumination source was measured using the internal Deuterated Triglycine

448 Sulfate (DTGS) detector of the FTIR with identical measurement conditions.

449 The photoresponse was calibrated using a NIST traceable Ge photodiode

450 (ThorLabs) with a 100 μm aperture placed in the same position as the device

451 under measurement. The frequency response of the devices was measured

452 using a directly modulated 1550 nm laser diode. Further details and a

453 schematic of the measurement setup are provided in ref. 35.

454
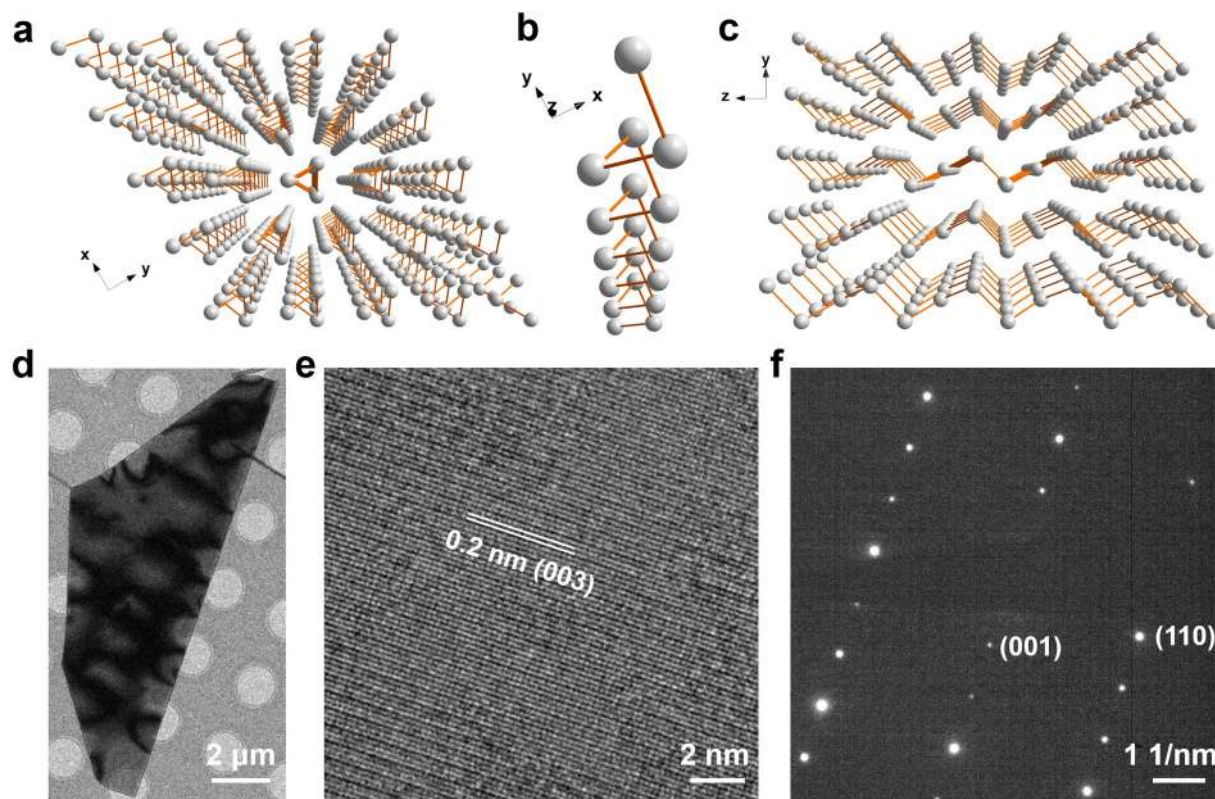
Figure 1. Crystal structure of tellurium: (a) viewed from x-axis, (b) single-molecular chain and (c) viewed from z-axis. (d) TEM image, (e) corresponding HR-TEM image and (f) SAED pattern of a typical tellurium nanoflake.

461
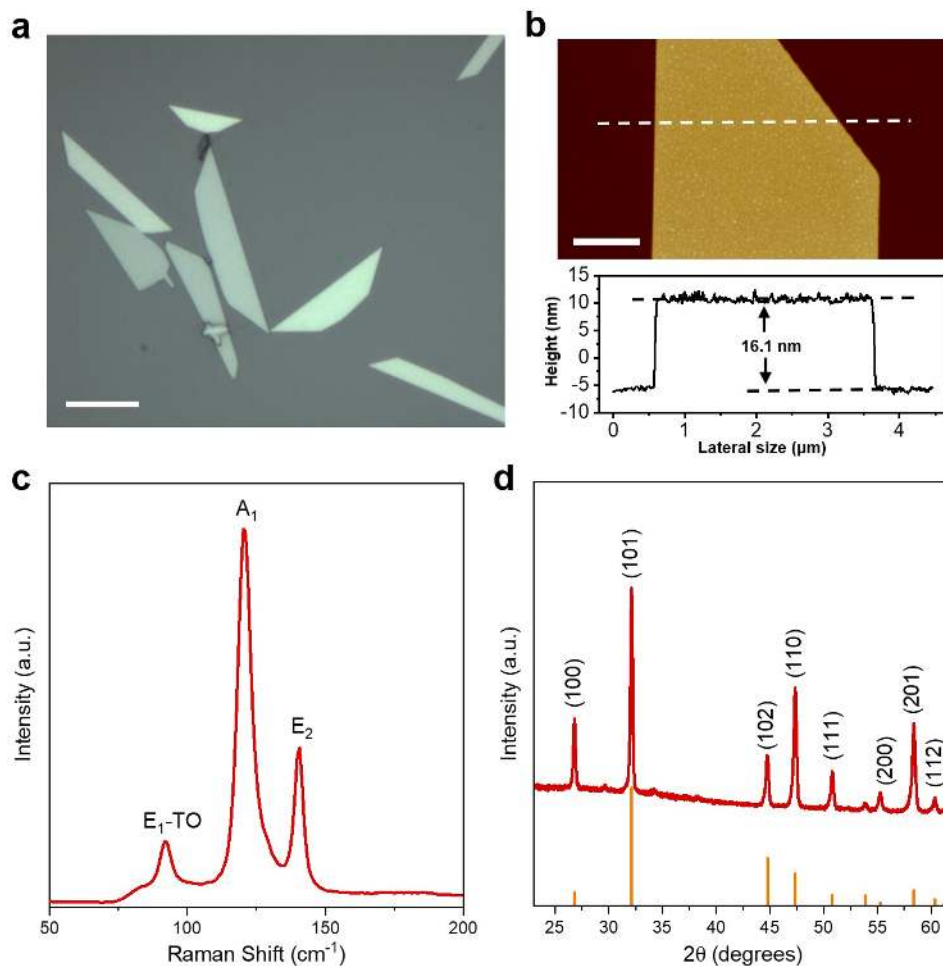
Figure 2. (a) Optical microscope image of tellurium nanoflakes deposited on a SiO$_2$/Si substrate, scale bar is 10 μm. (b) AFM image of typical tellurium nanoflake (top) and the corresponding height profile (bottom), scale bar is 1 μm. (c) Raman spectrum of tellurium nanoflakes. (d) XRD pattern of dried tellurium nanoflake powder.

467
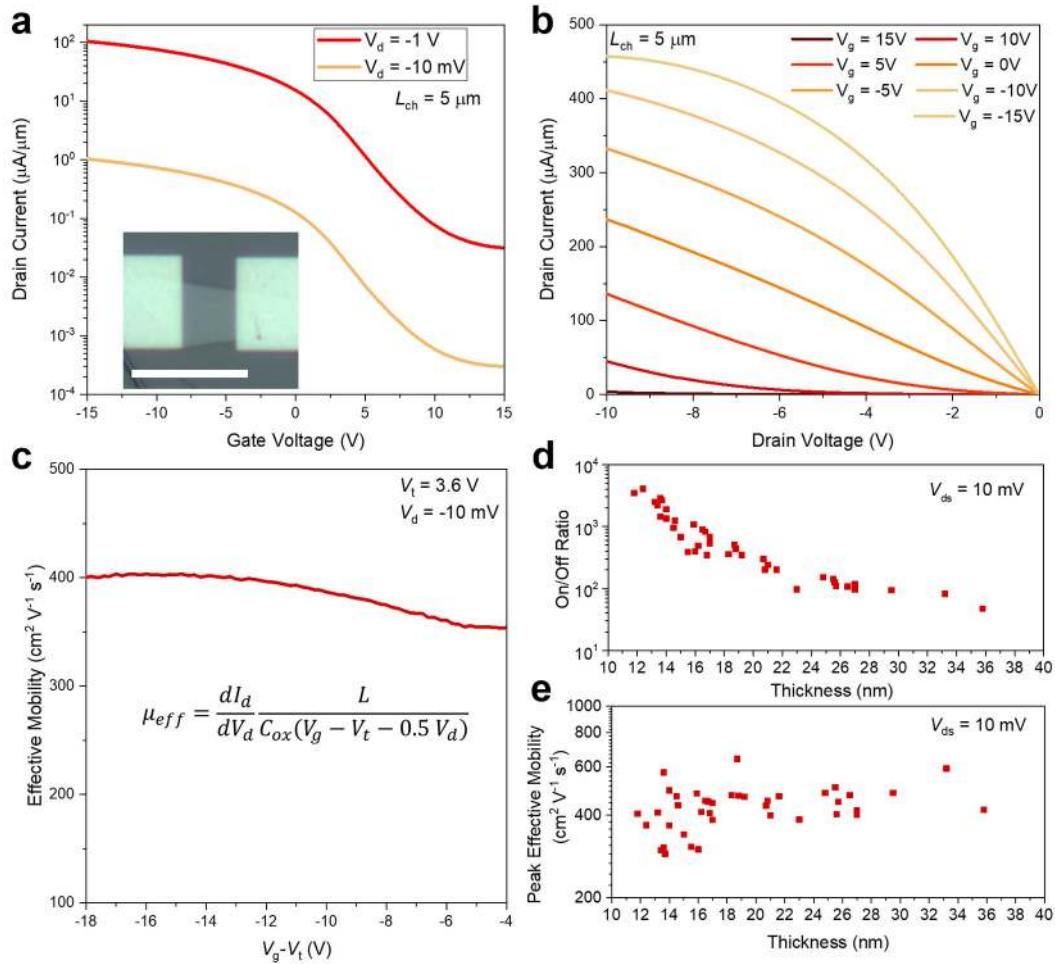
Figure 3. (a) Back-gated I_d-V_g characteristics of a 12.3 nm thick Te nanoflake with Pd contacts on 50 nm SiO_2 measured at room temperature; inset shows optical image of the device, scale bar is 10 μm. (b) I_d-V_d measured for the same device as shown in panel (a). (c) Effective mobility as a function of gate overdrive voltage for the device shown in panel (a) under a V_d of -10 mV, giving a peak mobility value of 619 cm^{-2} V^{-1} s^{-1}. (d) Thickness dependence of the on/off ratio measured for Te nanoflakes of varying thickness in the range of 12-36 nm. (e) Thickness dependence of the peak effective mobility measured for Te nanoflakes of varying thickness in the range of 12-36 nm.

480
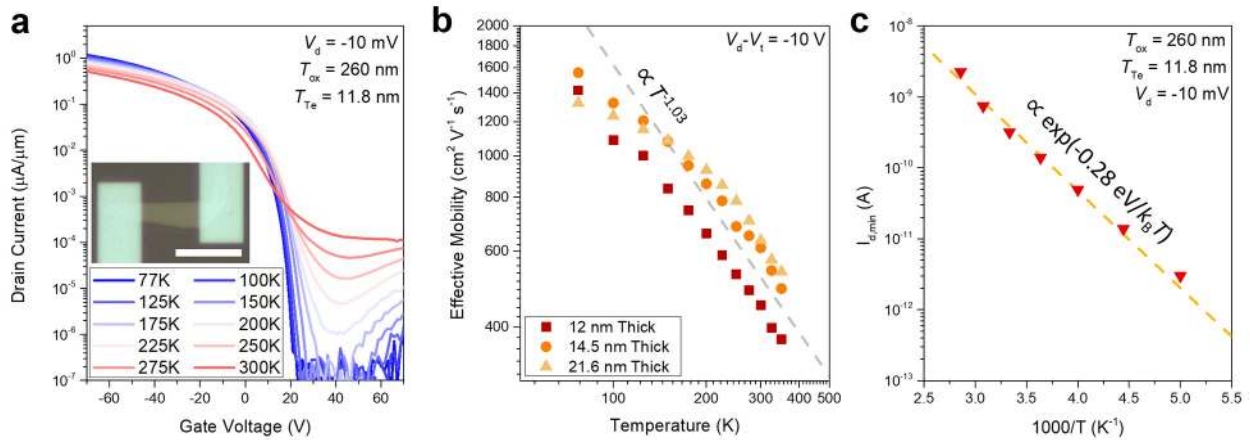
Figure 4. (a) Temperature dependent I_d-V_g characteristics of a 12 nm thick

Te nanoflake, measured at a low V_d of -10 mV. Scale bar is 5 μm. (b)

Effective mobility for quasi-2D Te nanoflakes with varying thickness as a

function of temperature extracted from panel (a) and Figure S1 at a constant

gate overdrive voltage of -10 V, dashed line shows a power law fit. (c)

Arrhenius plot showing the minimum drain source current ($I_{d,min}$) as a function

of temperature extracted from the data shown in panel (a).

488

489
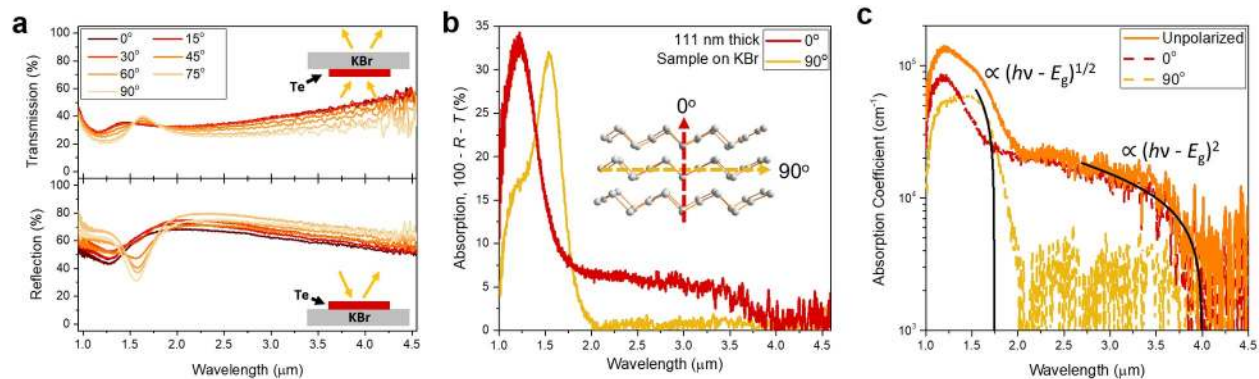
Figure 5. (a) Polarization resolved transmission and reflection spectra measured for a 111 nm thick Te nanoflake transferred on a KBr substrate, insets show the optical configuration used during measurements. (b) Absorption spectra for the nanoflake measured in panel (a), calculated from 100%-T-R. Inset shows the Te crystal directions of 0° and 90°. (c) Absorption coefficient of tellurium for unpolarized light, as well as light aligned parallel to z-axis (0°) and y-axis (90°) of Te crystal; Tauc plots and optical bandgap extraction for light polarized perpendicular and parallel to the wire axis are shown in Figure S2.

499
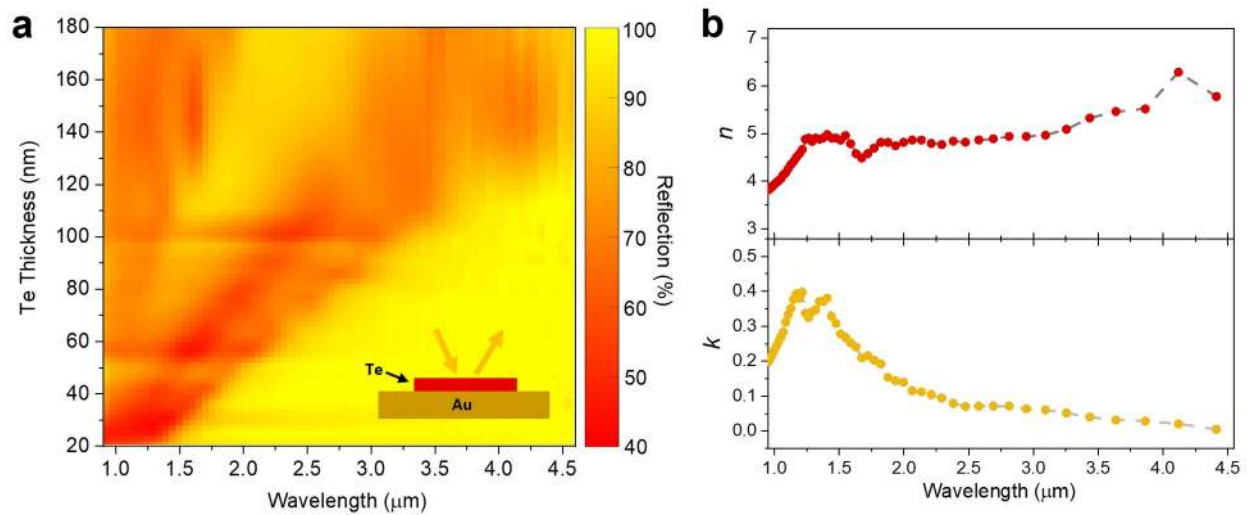
Figure 6. (a) Reflection of quasi-2D Te nanoflakes on Au substrates, with Te thickness ranging from 20 nm to 180 nm. Plot is obtained from interpolation of spectra taken on 18 Te crystal nanoflakes of varying thicknesses, shown in Figure S3. (b) Complex refractive index of quasi-2D Te nanoflakes calculated by fitting measured reflection data as a function of thickness.

505
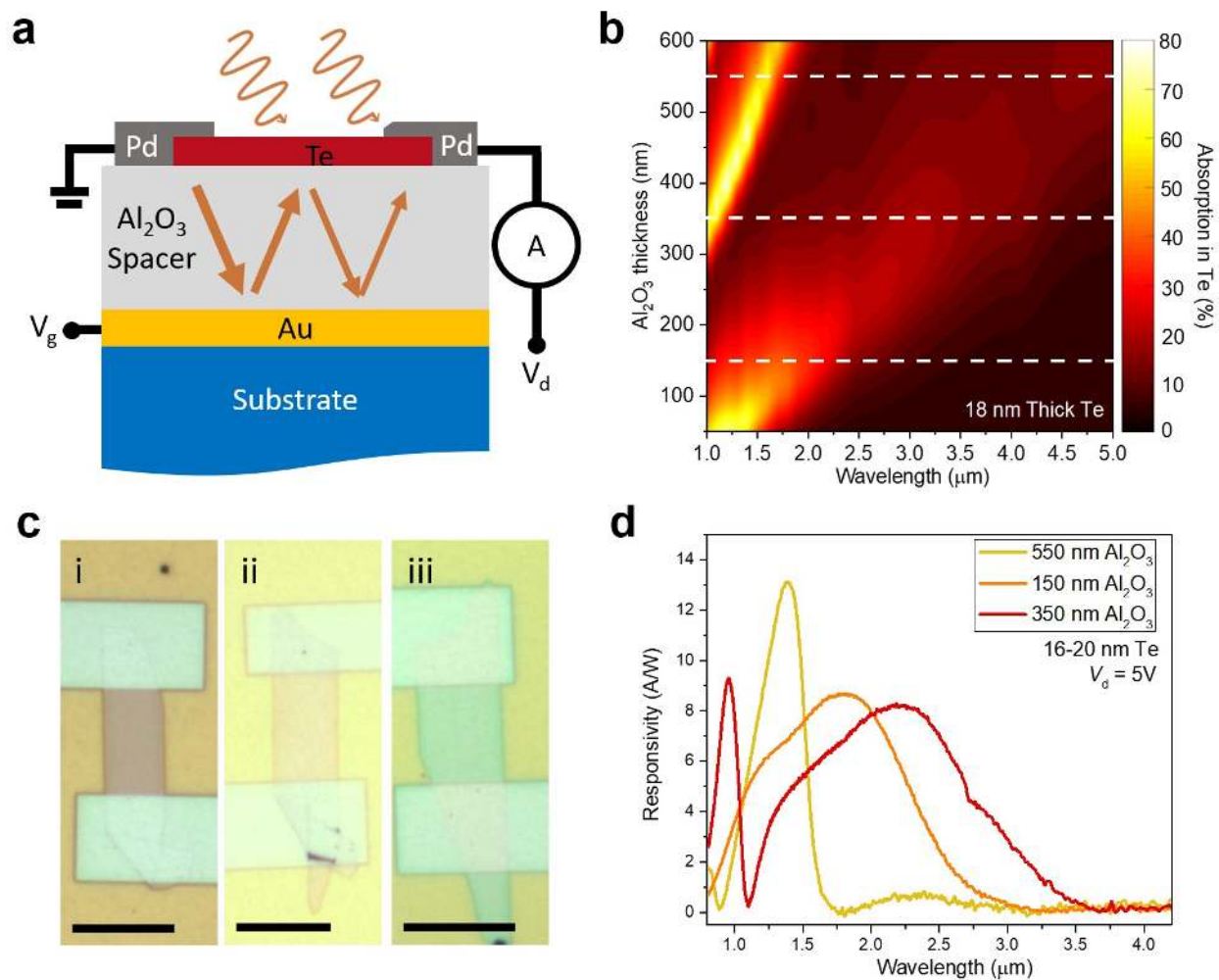
Figure 7. (a) Schematic showing the optical cavity structure used to fabricate SWIR photoconductors from quasi-2D Te nanoflakes in this study. An evaporated Au film acts as the gate electrode and back-reflector, while a Al_2O_3 dielectric layer acts as a $\sim\lambda/4$ spacer as well as the gate oxide. (b) Calculated absorption in the Te layer, as a function of wavelength and Al_2O_3 thickness for a fixed semiconductor thickness of 18 nm. (c) Optical images of SWIR photoconductors fabricated on optical cavities with Al_2O_3 thickness of 550 nm (i), 150 nm (ii), and 350 nm (iii); scale bar is 10 μm. (d) Measured

515   responsivities of quasi-2D Te nanoflakes fabricated on optical cavities with

516   different Al_2O_3 thicknesses.

517
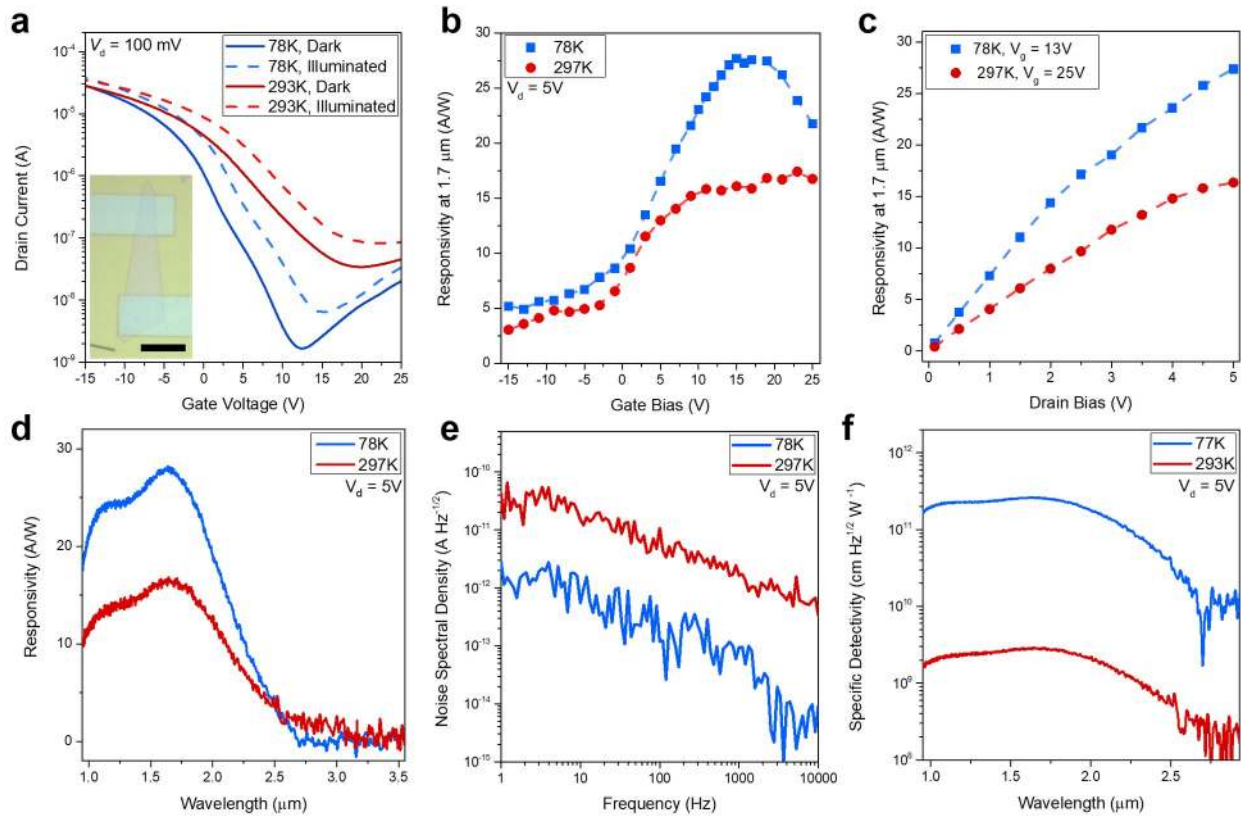
Figure 8. (a) I_d-V_g characteristics of an 18.8 nm Te photoconductor measured at 297K and 78K under illumination and in the dark. Inset shows optical image of the measured device; scale bar is 10 μm. (b) Responsivity at 1.7 μm measured at 297K and 78K as a function of gate bias, at a constant drain bias of V_d = 5 V. (c) Responsivity at 1.7 μm measured at 297K and 78K as a function of drain bias at an optimized gate bias (V_g = 13 V at 78K and V_g = 25 V at 297K). (d) Spectral responsivity per watt of a Te photoconductor measured at 78K and 297K under optimized gate bias and V_d = 5 V. (e) Noise spectrum measured at room temperature for a Te photoconductor operated with optimized gate bias and a V_d = 5 V and optimized gate bias. (f) Specific detectivity of Te photoconductors with optimized thickness; measurements were performed under gating conditions which maximized detectivity for the

29

531 specific device at room temperature. Note that an Au/Al$_2$O$_3$ substrate with an

532 Al$_2$O$_3$ thickness of 150 nm was used for the measurements.

533
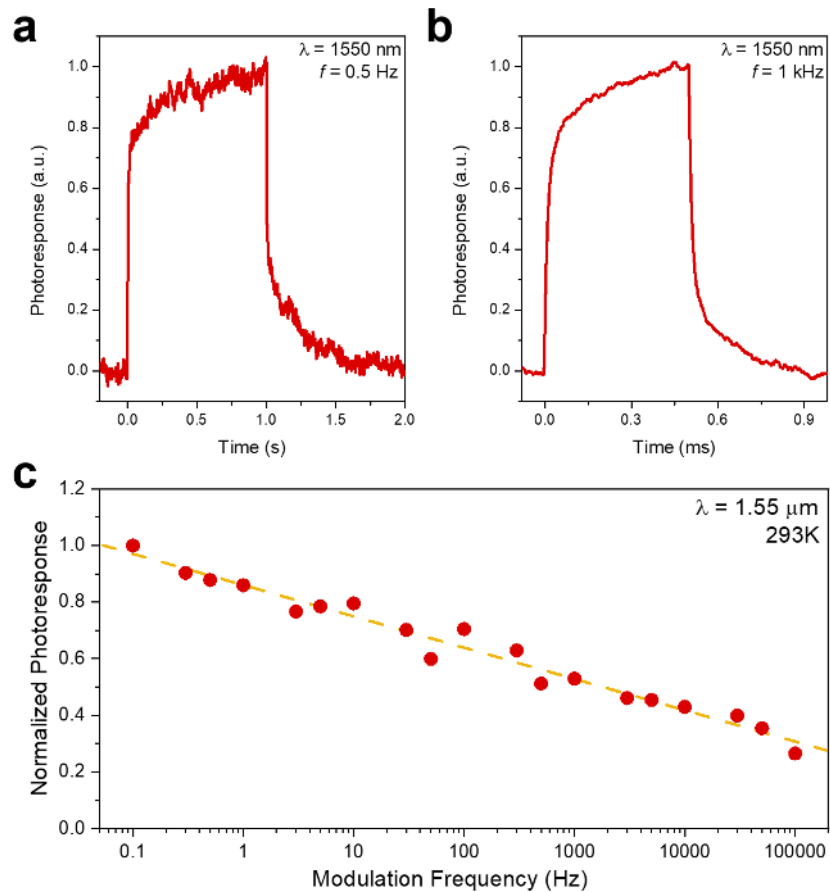
534
535 **Figure 9.** (a) Room-temperature step response of an 18.8nm thick Te

536 photoconductor, excited by a 1550-nm laser modulated by a 0.5 Hz square

537 wave. (b) Room-temperature step response of a Te photoconductor, excited

538 by a 1550 nm laser modulated by a 1 kHz square wave. (c) Normalized

539 photoresponse of a Te photoconductor *versus* modulation frequency; the

540 device is excited using a sinusoidally modulated 1550 nm laser. Note that an

541 Au/Al$_2$O$_3$ substrate with an Al$_2$O$_3$ thickness of 150 nm was used for the
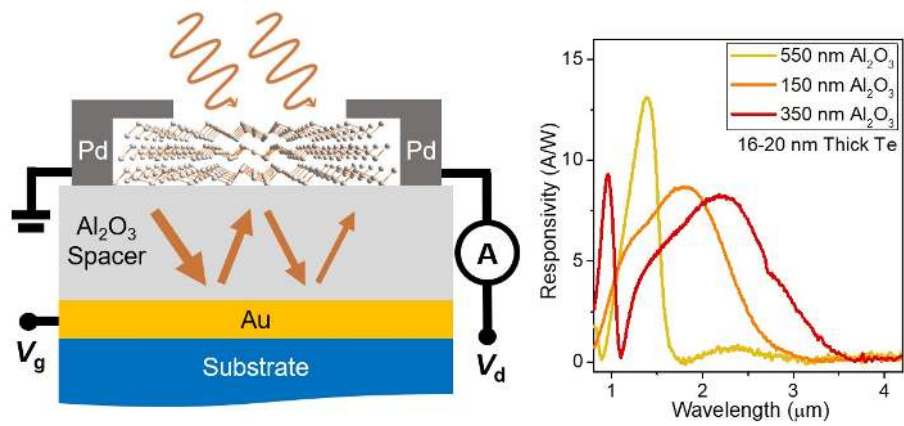
542 measurements.

543

544

545
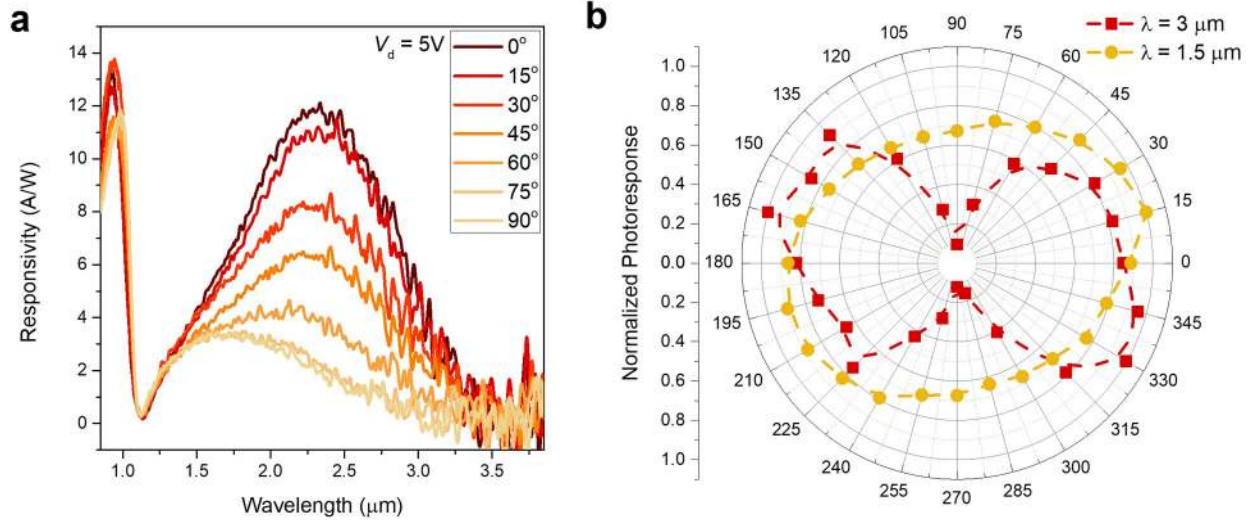
Figure 10. (a) Polarization resolved photoresponse of an 18.8 nm thick

quasi-2D Te nanoflake fabricated on an optical cavity with a 350 nm thick

Al_2O_3. (b) Polar plot showing the relative response of the device shown in

panel (a) at wavelengths of 3 μm and 1.5 μm as a function of polarization.

550

551 **TOC Graphic**

552

553

ASSOCIATED CONTENT

Supporting Information

The Supporting Information is available free of charge on the ACS Publications website.

Temperature dependent electrical characterization of additional devices. Tauc plot used to extract direct and indirect bandgap of Te. Reflection spectra used to create plot in Fig. 6a. Photoresponse measurements for devices prepared on Si/SiO_2 substrates. Reflection spectra taken on Te photoconductors.

AUTHOR INFORMATION

Corresponding Author

*E-mail: ajavey@berkeley.edu

ORCID

Matin Amani: 0000-0002-7912-6559

Chaoliang Tan: 0000-0003-1695-5285

George Zhang: 0000-0002-1741-5267

James Bullock: 0000-0001-7903-9642

Xiaohui Song: 0000-0001-7713-1373

Vivek Raj Shrestha: 0000-0002-7731-7677

Yang Gao: 0000-0002-9004-8483

Kenneth Crozier: 0000-0003-0947-001X

Mary Scott: 0000-0002-9543-6725

Ali Javey: 0000-0001-7214-7931

588

References

1. Alamo, J. A. Nanometre-Scale Electronics with III-V Compound Semiconductors. *Nature* **2011**, 479, 317-323.

2. Chuang, S.; Gao, Q.; Kapadia, R.; Ford, A. C.; Guo, J.; Javey, A. Ballistic InAs Nanowire Transistors. *Nano Lett.* **2012**, 13, 555-558.

3. Barve, A. V.; Lee, S. J.; Noh, S. K.; Krishna, S. Review of Current Progress in Quantum Dot Infrared Photodetectors. *Laser Photon. Rev.* **2009**, 4, 738-750.

4. Hoang, A. M.; Dehzangi, A.; Adhikary, S.; Razeghi, M. High Performance Bias-Selectable Three-Color Short-Wave/Mid-Wave/Long-Wave in Infrared Photodetecotrs based on Type-II InAs/GaSb/AlSb Superlattices. *Sci. Rep.* **2016**, 6, 24144.

5. Martyniuk, P.; Antoszewski, J.; Martyniuk, M.; Faraone, L.; Rogalski, A. New Concepts in Infrared Photodetector Designs. *Appl. Phys. Rev.* **2014**, 1, 041102.

6. Martinelli, R. U.; Zamerowski, T. J.; Longeway, P. A. 2.6 µm InGaAs Photodiodes. *Appl. Phys. Lett.* **1988**, 53, 989-991.

7. Nishida, K.; Taguchi, K.; Matsumoto, Y. InGaAsP Heterostructure Avalanche Photodiodes With High Avalanche Gain. *Appl. Phys. Lett.* **1979**, 35, 251-253.

8. Chen, K.; Kapadia, R.; Harker, A.; Desai, S.; Kang, J. S.; Chuang, S.; Tosun, M.; Sutter-Fella, C. M.; Tsang, M.; Zeng, Y.; Kiriya, D.; Hazra, J.; Madhvapathy, S. R.; Hettick, M.; Chen, Y.-Z.; Mastandrea, J.; Amani, M.; Cabrini, S.; Chueh, Y.-L.; Ager, J. W.; Chrzan, D. C.; Javey, A. Direct Growth

of Single Crystalline III-V Semiconductors on Amorphous Substrates. *Nat. Comm.* **2016**, 7, 10502.

9. Ko, H.; Takei, K.; Kapadia, R.; Chuang, S.; Fang, H.; Leu, P. W.; Ganapathi, K.; Plis, E.; Chen, S.-Y.; Madsen, M.; Ford, A. C.; Chueh, Y.-L.; Krishna, S.; Salahuddin, S.; Javey, A. Ultrathin Compound Semiconductor on Insulator Layers for High-Performance Nanoscale Transistors. *Nature* **2010**, 468, 286-289.

10. Fitzgerald, E. A.; Xie, Y.-H.; Monroe, D.; Silverman, P. J.; Kuo, J. M.; Kortan, A. R.; Thiel, F. A.; Weir, B. E. Relaxed Ge_xSi_{1-x} Structures for III-V Integration with Si and High Mobility Two-Dimensional Electron Gasses in Si. *J. Vac. Sci. Technol. B* **1992**, 10, 1807-1819.

11. Kim, Y.; Cruz, S. S.; Lee, K.; Alawode, B. O.; Choi, C.; Song, Y.; Johnson, J. M.; Heidelberger, C.; Kong, W.; Choi, S.; Qiao, K.; Almansouri, I.; Fitzgerald, E. A.; Kong, J.; Kolpak, A. M.; Hwang, J.; Kim, J. Remote Epitaxy Through Graphene Enables Two-Dimensional Material-Based Layer Transfer. *Nature* **2017**, 554, 340-343.

12. Li, T.; Cheng, J.-F.; Shao, X.-M.; Deng, H.-H.; Chen, Y.; Tang, H.-J.; Li, X.; Gong, H.-M. Performance of Low Dark Current InGaAs Shortwave Infrared Detector. *Proc. SPIE.* **2012**, 8419.

13. Tan, C.; Cao, X.; Wu, X.-J.; He, Q.; Yang, J.; Zhang, X.; Chen, J.; Zhao, W.; Han, S.; Nam, G.-H.; Sindoro, M.; Zhang, H. Recent Advances in Ultrathin Two-Dimensional Materials. *Chem. Rev.* **2017**, 117, 6225-6331.

14. Lin, Z.; McCreary, A.; Briggs, N.; Subramanian, S.; Zhang, K.; Sun, Y.; Li, X.; Borys, N. J.; Yuan, H.; Fullerton-Shirey, S. K.; Chernikov, A.; Zhao, H.;

McDonnell, S.; Lindenberg, A. M.; Xiao, K.; LeRoy, B. J.; Drndić, M.; Hwang, J. C.M.; Park, J.; Chhowalla, M.; *et al*. 2D Materials Advances: From Large Scale Synthesis and Controlled Heterostructures to Improved Characterization Techniques, Defects and Applications. *2D Mater*. **2016**, 3, 042001.

15.   Amani, M.; Lien, D.-H.; Kiriya, D.; Xiao, J.; Azcatl, A.; Noh, J.; Madhvapathy, S. R.; Addou, R.; Kc, S.; Dubey, M.; Cho, K.; Wallace, R. M.; Lee, S.-C.; He, J.-H.; Ager, J. W.; Zhang, X.; Yablonovitch, E.; Javey, A. Near-Unity Photoluminescence Quantum Yield in MoS_2. *Science* **2015**, 350, 1065-1068.

16.   Amani, M.; Taheri, P.; Addou, R.; Ahn, G. H.; Kiriya, D.; Lien, D.-H.; Ager, J. W.; Wallace, R. M.; Javey, A. Recombination Kinetics and Effects of Superacid Treatment in Sulfur- and Selenium Based Transition Metal Dichalcogenides. *Nano Lett.* **2016**, 16, 2786-2791.

17.   Desai, S. B.; Madhvapathy, S. R.; Sachid, A. B.; Llinas, J. P.; Wang, Q.; Ahn, G. H.; Pitner, G.; Kim, M. J.; Bokor, J.; Hu, C.; Wong, H.-S. P.; Javey, A. MoS_2 Transistors with 1-Nanometer Gate Lengths. *Science* **2016**, 354, 99-102.

18.   Lien, D.-H.; Amani, M.; Desai, S. B.; Ahn, G. H.; Han, K.; He, J.-H.; Ager, J. W.; Wu, M. C.; Javey, A. Large-Area and Bright Pulsed Electroluminescence in Monolayer Semiconductors. *Nat. Comm.* **2018**, 9, 1299.

19.   Zhang, Y. J.; Oka, T.; Suzuki, R.; Ye, J. T.; Iwasa, Y. Electrically Switchable Chiral Light-Emitting Transistor. *Science* **2014**, 344, 725-728.

661   20.   Zhao, P.; Amani, M.; Lien, D.-H.; Ahn, G. H.; Kiriya, D.; Mastandrea, J. P.;

662   Ager, J. W.; Yablonovitch, E.; Chrzan, D. C.; Javey, A. Measuring the Edge

663   Recombination Velocity of Monolayer Semiconductors. *Nano Lett.* **2017**,

664   17, 5356-5360.

665   21.   Wang, Y.; Qiu, G.; Wang, R.; Huang, S.; Wang, Q.; Liu, Y.; Du, Y.;

666   Goddard, W. A.; Kim, M. J.; Xu, X.; Ye, P. D.; Wu, W. Field-Effect Transistors

667   made from Solution-Grown Two-Dimensional Tellurene. *Nat. Electron.*

668   **2018**, 1, 228-236.

669   22.   von Hippel, A. Structure and Conductivity in the VIb Group of the

670   Periodic System. *J. Chem. Phys.* **1948**, 16, 372-380.

671   23.   Yi, S.; Zhu, Z.; Cai, X.; Jia, Y.; Cho, J.-H. The Nature of Bonding in Bulk

672   Tellurium Composed of One-Dimensional Helical Chains. *Inorg. Chem.*

673   **2018**, DOI: 10.1021/acs.inorgchem.7b03244.

674   24.   Wu, B.; Liu, X.; Yin, J.; Lee, H. Bulk β-Te to Few Layered β-Tellurenes:

675   Indirect to Direct Band-Gap Transitions Showing Semiconductor Property.

676   *Mater. Res. Express* **2017**, 4,095902.

677   25.   Qian, H.; Yu, S.; Gong, J.; Luo, L.; Fei, L. High-Quality Luminescent

678   Tellurium Nanowires of Several Nanometers in Diameter and High Aspect

679   Ratio Synthesized by a Poly(Vinyl Pyrrolidone)-Assisted Hydrothermal

680   Process. *Langmuir* **2006**, 22, 3830-3835

681   26.   Du, Y.; Qiu, G.; Wang, Y.; Si, M.; Xu, X.; Wu, W.; Ye, P. D. 1D van der

682   Waals Material Tellurium: Raman Spectroscopy under Strain and Magneto-

683   transport

684   Source. *Nano Lett.* **2017**, 17, 3965-3973.

685   27.   Liu, H.; Neal, A. T.; Zhu, Z.; Luo, Z.; Xu, X.; Tomanek, D.; Ye, P. D.

686   Phosphorene: An Unexplored 2D Semiconductor with a High Hole Mobility.

687   *ACS Nano* **2014**, 8, 4033-4041.

688   28.   Li, L.; Yu, Y.; Ye, G. J.; Ge, Q.; Ou, X.; Wu, H.; Feng, D.; Chen, X. H.;

689   Zhang, Y. Black Phosphorus Field-Effect Transistors. *Nat. Nano.* **2014**, 9,

690   372-377.

691   29.   Takei, K.; Madsen, M.; Fang, H.; Kapadia, R.; Chuang, S.; Kim, H. S.; Liu,

692   C.-H.; Plis, E.; Nah, J.; Krishna, S.; Chueh, Y.-L. Guo, J.; Javey, A. Nanoscale

693   InGaSb Heterostructure Membranes on Si Substrates for High Hole

694   Mobility Transistors. *Nano Lett.* **2012**¸12, 2060-2066.

695   30.   Radisavljevic, B.; Kis A. Mobility Engineering and a Metal-Insulator

696   Transition in Monolayer MoS_2. *Nat. Matter.* **2013**, 12, 815-820.

697   31.   Javey, A.; Guo, J.; Farmer, D. B.; Wang, Q.; Wang, D.; Gordon, R. C.;

698   Lundstrom, M.; Dai, H. Carbon Nanotube Field-Effect Transistors with

699   Integrated Ohmic Contacts and High-κ Gate Dielectrics. *Nano Lett.* **2004**,

700   4, 447-450.

701   32.   Lien, D.-H.; Kang, J. S.; Amani, M.; Chen, K.; Tosun, M.; Wang, H.-P.; Roy,

702   T.; Eggleston, M. S.; Wu, M. C.; Dubey, M.; Lee, S.-C.; He, J.-H.; Javey, A.

703   Engineering Light Outcoupling in 2D Materials. *Nano Lett.* **2015**, 15, 1356-

704   1361.

705   33.   Zhang, H.; Ma, Y.; Wan, Y.; Rong, X.; Xie, Z.; Wang, W.; Dai, L. Measuring

706   the Refractive Index of Highly Crystalline, Monolayer MoS_2 with High

707   Confidence. *Sci. Rep.* **2015**, 5, 8440.

708   34.   Born, M.; Wolf. E. Principles of optics: Electromagnetic Theory of

Propagation, Interference and Diffraction Light. Cambridge University Press, Cambridge (2002).

35.   Amani, M.; Regan, E.; Bullock, J.; Ahn, G. H.; Javey, A. Mid-Wave Infrared Photoconductors based on Black Phosphorous-Arsenic Alloys. *ACS Nano* **2017**, 11, 11724-11731.

36.   Guo, Q.; Pospischil, A.; Bhuiyan, M. Jiang, H.; Tian, H.; Farmer, D.; Deng, B.; Li, C.; Han, S.-J.; Wang, H.; Xia, Q.; Ma, T.-P. Mueller, T.; Xia, F. Black Phosphorus Mid-Infrared Photodetectors with High Gain. *Nano Lett.* **2016**, 16, 4648-4655.

37.   Piotrowski, J.; Gawron, W. Ultimate Performance of Infrared Photodetectors and Figure of Merit of Detector Material. *Infar. Phys. Technol.* **1997**, 38, 63-68.

38.   Vincent, J. D. Fundamentals of Infrared Detector Operation and Testing. Wiley, New York (1990).

39.   Petritz, R. L. Theory of Photoconductivity in Semiconductor Film. *Phys. Rev.* **1956**, 104, 1508-1516.

40.   Beck, W. A. Photoconductive Gain and Generation-Recombination Noise in Multiple-Quantum-Well Infrared Detectors. *Appl. Phys. Lett.* **1993**, 63, 3589-3591.

41.   Ye, Z.; Campbell, J. C.; Chen, Z.; Kim, E.-T., Madhukar, A. Noise and Photoconductive Gain in InAs Quantum-Dot Infrared Photodetectors. *Appl. Phys. Lett.* **2003**, 83, 1234-1236.